



## Permeability measurements and modeling of topology-optimized metallic 3-D woven lattices

Longyu Zhao,<sup>a,\*</sup> Seunghyun Ha,<sup>b</sup> Keith W. Sharp,<sup>c</sup> Andrew B. Geltmacher,<sup>d</sup> Richard W. Fonda,<sup>d</sup> Alex H. Kinsey,<sup>a</sup> Yong Zhang,<sup>e</sup> Stephen M. Ryan,<sup>a</sup> Dinc Erdeniz,<sup>f</sup> David C. Dunand,<sup>f</sup> Kevin J. Hemker,<sup>e,a</sup> James K. Guest<sup>b</sup> and Timothy P. Weihs<sup>a,e</sup>

<sup>a</sup>Department of Materials Science and Engineering, Johns Hopkins University, 3400 N Charles Street, Baltimore, MD 21218, USA

<sup>b</sup>Department of Civil Engineering, Johns Hopkins University, 3400 N Charles Street, Baltimore, MD 21218, USA

<sup>c</sup>SAERTEX USA, LLC, Huntersville, NC 28078, USA

<sup>d</sup>Multifunctional Materials Branch, Code 6350, US Naval Research Laboratory, 4555 Overlook Ave SW, Washington, DC 20375, USA

<sup>e</sup>Department of Mechanical Engineering, Johns Hopkins University, 3400 N Charles Street, Baltimore, MD 21218, USA

<sup>f</sup>Department of Materials Science and Engineering, Northwestern University, 2220 Campus Drive, Evanston, IL 60208, USA

Received 7 May 2014; revised 8 August 2014; accepted 18 August 2014

Available online 18 September 2014

**Abstract**—Topology optimization was combined with a 3-D weaving technique to design and fabricate structures with optimized combinations of fluid permeability and mechanical stiffness. Two different microarchitected structures are considered: one is a “standard” weave in which all wires were included, while the other is termed an “optimized” weave as specific wires were removed to maximize the permeability of the resulting porous materials with only a limited reduction in stiffness. Permeability was measured and predicted for both structures that were 3-D woven with either Cu or Ni–20Cr wires. The as-woven wires in the Cu lattices were bonded at contact points using solder or braze while the Ni–20Cr wires were bonded at contact points using pack aluminization. Permeability was measured under laminar flow conditions in all three normal directions for unbonded and bonded samples and in the optimized structure it was found to increase between 200% and 600%, depending on direction, over the standard structures. Permeability was also predicted using finite-element modeling with as-fabricated wires positions that were identified with optical microscopy or X-ray tomography; the measurements and predictions show good agreement. Lastly, the normalized permeability values significantly exceed those found for stochastic, metallic foams and other periodic structures with a material volume fraction of over 30%.  
© 2014 Acta Materialia Inc. Published by Elsevier Ltd. All rights reserved.

**Keywords:** 3-D woven lattices; Permeability; Topology optimization; Finite-element modeling; X-ray tomography

### 1. Introduction

Cellular materials offer the exciting opportunity to enhance fluidic, thermal and mechanical properties when fabricated as either stochastic structures such as metal foams [1–5] or periodic structures such as prismatic topologies [6–8], truss architectures [9–12] or woven textiles [13–15]. Stochastic structures provide excellent heat exchange [3,4,16] and energy absorption [17,18] due to their large specific surface areas and light weight, but their low stiffness and strength limit use in load-bearing applications [19,20]. Periodic structures with regular topologies have been studied as alternatives that offer more stiffness and strength while still enabling the exchange of heat and the absorption of energy [21–23]. As examples, Maloney

et al. [24] investigated a microlattice heat exchanger that possesses high compressive strength and energy absorption; Wadley [25] presented truss topologies that support high stresses, enable cross flow heat exchange and mitigate dynamic loads; and Wirtz and Park et al. [13,14] examined thermal and fluid flow in 2-D screen laminates and 3-D metal textile sheets. In this study we explore similar periodic structures but have gone one step further by trying simultaneously to optimize two coupled properties: fluid permeability and mechanical stiffness. Both properties can be important for applications such as filters, actuators [26], porous bone implant scaffolds [27–29] and heat exchangers [30]. These two properties are competing as increases in porosity may enhance permeability but degrade stiffness [31,32]. To design a periodic structure with the best combination of permeability and stiffness, we utilize topology optimization that can identify an ideal material architecture that yields the best combination of considered properties. We draw on earlier efforts [31–33] that proposed

\* Corresponding author. Tel.: +1 (410)516 4274; fax: +1 (410)516 5293; e-mail: [longyu@jhu.edu](mailto:longyu@jhu.edu)

optimized 3-D porous structures but in this paper we focus exclusively on optimized topologies that can be manufactured via the 3-D weaving process [34,35].

Topology optimization has proven to be extremely effective in designing new structural materials, yet the technique tends to produce complex architectures that may be challenging to manufacture [36]. The Heaviside Projection Method [37] is a well-known approach in topology optimization and is capable of improving manufacturability by controlling the length scale of designed features in (for example) porous [32,38] and composite materials [39]. In related research, this Heaviside Projection Method was extended to 3-D woven materials to ensure topology-optimized lattices were manufacturable. By including weaving constraints within the topology optimization routine, we were able to predict orthogonal, periodic structures in which wires were removed to enhance permeability in particular directions, with only a limited decrease in stiffness. The basic weaving process is shown in Fig. 1a [34], with metallic wires extending in all three directions, and with the through-thickness (Z) wires binding the warp (X) and fill (Y) wires. A finite-element (FE) model of a standard or baseline architecture is shown in Fig. 1c and an X-ray tomographic image is shown in Fig. 1d with all wires in place. Topology optimization suggested removing wires in the X and Y directions as shown in Fig. 1e and f to maximize the permeability in the X direction with limited decrease in stiffness. The resulting wave-like flow field is displayed in Fig. 1b. This optimized architecture is predicted to provide a 280% increase in permeability, with only a 15–30% drop in specific stiffness on going from the standard to the optimized weave [33].

Here we examine the as-fabricated woven architectures and quantify and predict their permeability in all three directions. To do so accurately, though, we do not rely solely on predictions from the optimization routines. Such predictions are based on ideal single cells that are extended to perfect, infinitely periodic material with no deviations in wire positions [40]. The assumption of perfect weaves without manufacturing defects leads to predictions that are much lower than the measured values. For accurate predictions of permeability in the as-fabricated structures, we must characterize and then account for manufacturing defects such as spreads in wiring spacing, as well as edge effects and fluid conditions. In this study we use optical microscopy to characterize average wire positions and X-ray tomographic studies to identify actual wire locations. These microstructure data are then input into FE models to predict permeability in all three directions, for comparison with measured values. (The stiffness of the woven samples is also measured but is reported elsewhere [41].) We consider both a standard and an optimized architecture that are woven using Cu or Ni–20Cr wires. After weaving, the Cu wires are bonded at contact points using solder or braze and the Ni–20Cr wires are bonded using pack aluminization. We quantify the permeabilities for unbonded and bonded samples in all three orthogonal directions under a laminar flow condition, and compare the measured values with the FE model predictions.

## 2. Experimental apparatus and procedures

Cu wires (Arcor Electronics) and Ni–20 wt.% Cr wires (Arcor Electronics) [42] with 202  $\mu\text{m}$  diameters were sepa-

rately 3-D woven into parts, shown in Fig. 2a, measuring 3 mm in thickness, 36 mm in width, and over 200 mm in length at North Carolina State University using a 3-D fabric machine owned by SAERTEX USA LLC [34]. Two different structures were fabricated, each with five warp layers and six fill layers: a standard weave in which pairs of wires run in the X and Y directions and single wires run in the Z direction (Fig. 1c and d), and a topology-optimized weave in which every other pair of wires is removed in the X and Y directions (Fig. 1e and f) so as to maximize permeability in the X direction. To prepare samples, we first cut strips from the full weaves  $\sim 20$  mm in length using electrical discharge machining (EDM) (Fig. 2b and c). Then, in order to fit in our testing holder and avoid the ragged edges shown in Fig. 2a, we cut  $16 \times 16 \times 3$  mm samples from the middle of strips to form unbonded samples (Fig. 2d). To create a rigid lattice, we bonded the wires using one of three methods. Cu wires are bonded using a standard SAC305 (96.5 wt.% Sn/3.0 wt.% Ag/0.5 wt.% Cu) solder sheets (Indium Corporation of America) [43] or AgCu (72 wt.% Ag/28 wt.% Cu) braze sheets (Lucas-Milhaupt alloy 721-VTG) [44], and the Ni–20Cr wires are bonded using pack aluminization [45,46]. Fig. 2d shows the finished samples after bonding and Fig. 2e–h show both unbonded and bonded wires.

For soldering, 50  $\mu\text{m}$  thick SnAgCu sheets were placed on top of the unbonded Cu weaves and the assemblies were heated at a rate of  $20 \text{ }^\circ\text{C min}^{-1}$  to  $500 \text{ }^\circ\text{C}$ , held for 10 min in a low vacuum ( $\sim 10^{-3}$  Torr), and then cooled to room temperature. Six or four layers of solder sheets were used for the standard or optimized samples, respectively, and no flux was required due to the low vacuum.

Given the temperature limitations of solders, we developed an analogous method of bonding with higher-temperature AgCu braze. Unbonded samples were sandwiched between 46  $\mu\text{m}$  thick foils of braze, heated at a rate of  $30 \text{ }^\circ\text{C min}^{-1}$  to  $900 \text{ }^\circ\text{C}$ , and held for 5 min to allow the sample to reach a uniform temperature under a 95 mol.%  $\text{N}_2$ /5 mol.%  $\text{H}_2$  forming gas atmosphere at 2 psig. Samples were then cooled to  $25 \text{ }^\circ\text{C}$ .

Pack aluminization, which is one of several chemical vapor deposition processes in which a vapor is formed and then deposits on a substrate through chemical reactions, has been used to coat nickel parts [47–49] and nickel foams [46,50,51]. Here we use it to deposit a 12  $\mu\text{m}$  thick, uniform NiAl coating on the woven Ni–20Cr wires [45] at  $1000 \text{ }^\circ\text{C}$  for 1 h, as described in detail elsewhere [52]. The NiAl coatings merged at numerous wire contact points to form nodes or solid-state bonds. After homogenization at  $1200 \text{ }^\circ\text{C}$  for 48 h, a final composition of Ni–19Cr–4Al is achieved, with no compositional gradients across wire diameters or across the bonds between adjacent wires.

To measure permeability in the X, Y and Z directions, we designed and fabricated the two stainless steel sample holders shown in Fig. 3a and b. In the X or Y directions, we sealed all four sides of the samples with Rogers BISCO silicone closed-cell foam to prevent leaks around the samples, as shown in Fig. 3b. As the compressed foams do exert pressure on the weaves we examined the impact of these loads on the permeability measurements using foams of different stiffness. In the Z direction, we used a double O-ring system as shown in Fig. 3c and d to ensure that fluid flows only in the Z direction and not around the sample. Given that the sample is thin (3 mm), we assume the inner

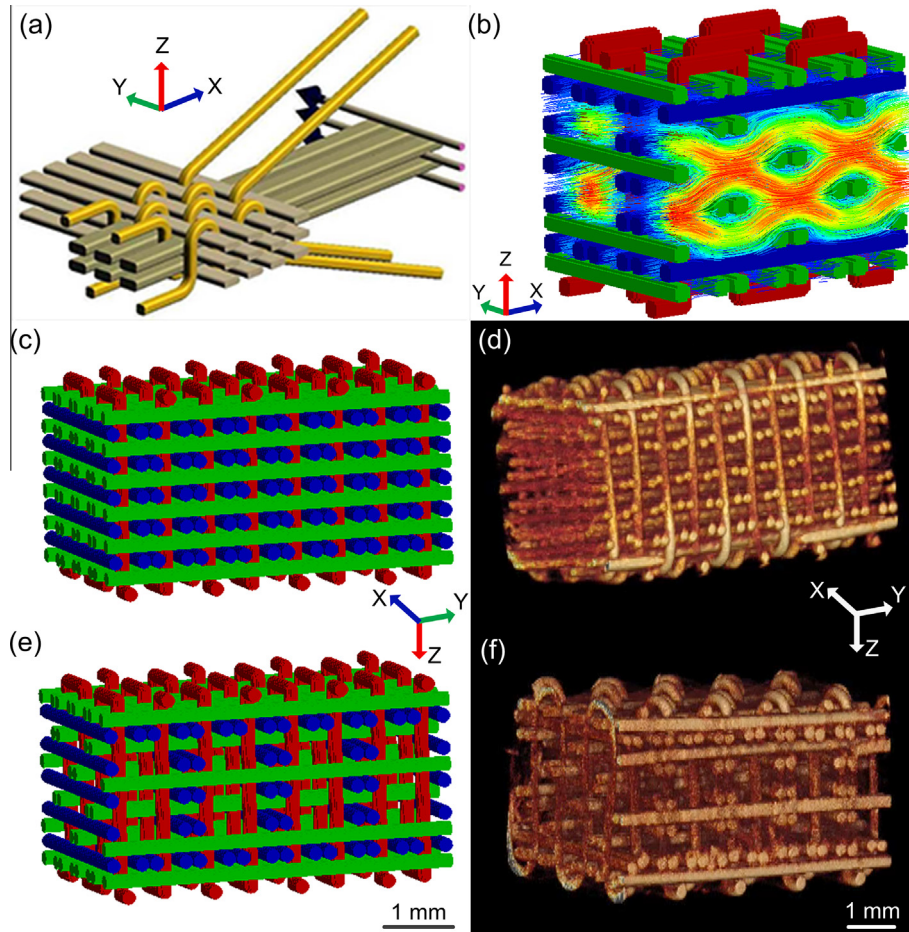


**Fig. 1.** (a) 3-D weaving process with warp (X), fill (Y) and z (Z) wires inserted in three orthogonal directions. (b) Topology-optimized wave-like flow pattern to achieve maximum permeability with limited drop in stiffness. (c, d) FEM model and X-ray tomographic images of the “standard” structure, respectively. (e, f) FEM model and X-ray tomographic images of the “optimized” structure, respectively. Note the removal of wires in the X and Y directions in the optimized structure.

diameter of the small O-ring defines the effective cross-sectional area for fluid flow.

Fig. 4 displays a schematic of the experimental setup for measuring permeability. Compressed air forces polyethylene glycol 400 (PEG, Sigma Aldrich) through the sample and the regulation valve is adjusted to an accuracy of  $\pm 0.05\%$  to control the rate of fluid flow. The dynamic viscosity of the PEG was measured independently to be 112.2 cP at 20 °C using a Brookfield LVDV-II+PRO viscometer. An OMEGA HHP-807/SIL differential pressuremeter is positioned immediately before and after the sample holder, and the pressure difference is measured to an accuracy of  $\pm 1.4$  kPa. Knowing the thickness of the sample, the pressure gradients were then calculated. Flow rates were measured using an OMEGA FPD1002B flowmeter with  $\pm 1\%$  accuracy, and flow velocities were calculated using the appropriate cross-sectional areas. When measuring permeability in the X and Y directions, areas were measured using cross-sectional optical images and ImageJ software. For the Z measurements, the inner diameter of the smaller O-ring was assumed to be the cross-sectional area:  $4.21 \times 10^{-5} \text{ m}^2$ .

To calculate permeability we measured the pressure drop for a series of flow rates and then applied Darcy’s law:

$$\nabla P = \frac{\Delta P}{L} = \frac{\mu}{K} v, \quad (1)$$

where  $\Delta P$  is the pressure drop across the sample,  $L$  is the sample thickness,  $\mu$  is the viscosity,  $K$  is the permeability, and  $v$  is the superficial velocity defined by the flow rate through the cross-section. Given that Darcy’s law approximates creeping laminar flows, we used the following equation to estimate the range of Reynolds numbers,  $Re$ , for our experiments:

$$Re = \frac{\rho D_h}{\mu} v, \quad (2)$$

where  $\rho$  is the density of fluid,  $D_h$  is the hydraulic diameter, and  $v$  is the superficial velocity defined as the ratio of the flow rate  $Q$  and the cross-sectional area  $A$ :

$$v = \frac{Q}{A}. \quad (3)$$

The hydraulic diameter,  $D_h$ , can be estimated for a 3-D woven structure by:

$$D_h = \frac{4\varepsilon}{\beta}, \quad (4)$$

where  $\varepsilon$  is the porosity of the material and  $\beta$  is the specific surface area, defined by the total surface area divided by the volume in a unit cell [13]. Knowing the diameters,  $d$ , of the wires in both the standard (*std*) and optimized (*opt*) geometries, the porosities and specific surface areas for both structures are computed based on geometry as:

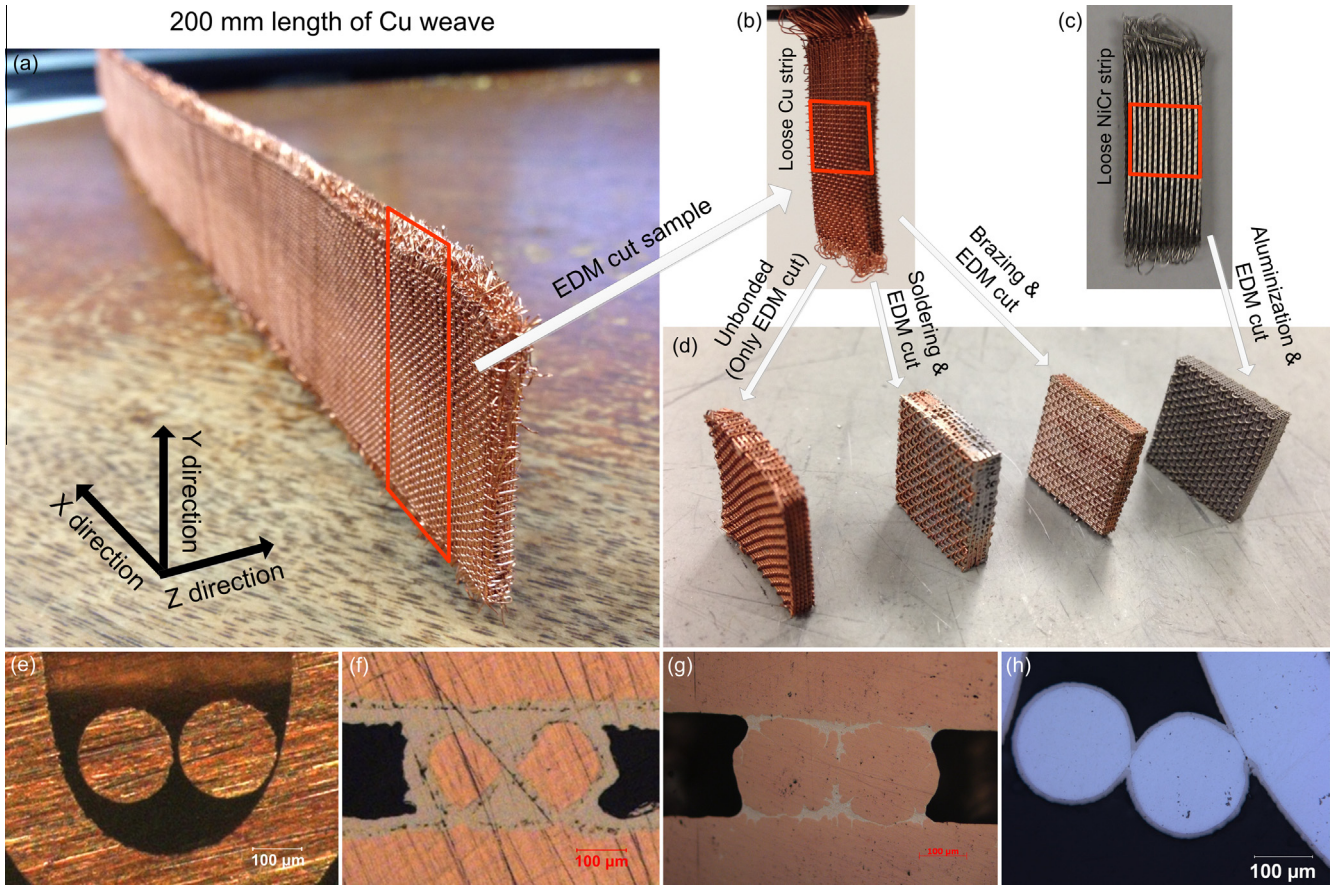


**Fig. 2.** (a) 3-D orthogonal weaves that measure 3 mm in thickness (Z direction), 36 mm in width (Y direction), and over 200 mm in length (X direction). (b, c) After fabrication, the weaves are cut into 20 mm lengths using electrical discharge machining (EDM) for the purpose of bonding. (d) Finished samples measuring  $16 \times 16 \times 3$  mm are then cut from the 20 mm strips using EDM. This includes both unbonded and bonded samples. Optical images of (e) unbonded wires as well as wires bonded by (f) soldering, (g) brazing and (h) pack aluminization.

$$\varepsilon_{std} = 0.4563, \quad \beta_{std} = \frac{2.175}{d}, \quad (5)$$

$$\varepsilon_{opt} = 0.5972, \quad \beta_{opt} = \frac{1.611}{d}. \quad (6)$$

Using these equations, the hydraulic diameters are then given as:

$$D_{h,std} = 0.839d, \quad D_{h,opt} = 1.483d. \quad (7)$$

Given that all wires have diameters  $d = 202 \mu\text{m}$ , the hydraulic diameters for ideal unbonded standard and optimized structures are 169 and  $300 \mu\text{m}$ , respectively. When accounting for actual wire spacings, which are larger than the theoretical values due to gaps in the manufactured samples, the hydraulic diameters increase to 297 and  $470 \mu\text{m}$ , respectively, and the Reynolds numbers range from 0.05 to 0.70 for the experiments reported here. Thus, laminar flow is confirmed and the use of Darcy's law is appropriate.

Two different finite-element method (FEM)-based approaches were used to model and predict permeabilities of the woven structures. The first approach used homogenization to approximate the effective permeability of unit cell architectures that are representative of the standard and optimized samples. As the weaving process introduced small, unintended spacings between wires, cross-sectional optical microscopy was used to determine the average spacing between wires. Idealized wire positions were then

adjusted accordingly by introducing small increments in spacing between relevant wires using multiples of the FEM mesh resolution,  $16.8 \mu\text{m}$ . A FEM-based implementation [40] of homogenization theory [53] was then used to estimate permeability.

The second FEM-based approach sought to model an actual specimen by determining exact wire locations using X-ray tomography. The X-ray tomography was performed with a Skyscan 1172 microtomography system. Using this system, acquiring tomographic scans of individual permeability specimens is difficult, due to the size and shape of the specimens ( $16 \times 16 \times 3.3$  mm). Therefore a single specimen was cut into three sections ( $16 \times 5.4 \times 3.3$  mm) using an abrasive cut-off wheel. The tomography of each section was additionally split into two scans consisting of the top and bottom of the section with significant overlap. Each scan was performed with a scan resolution of  $11.8 \mu\text{m}$ , and an angular step of  $0.2^\circ$  with the specimen rotated through  $180^\circ$ , resulting in 900 radiographs for each reconstruction. Each radiograph used in the reconstruction was the average of 20 measurements and small random vertical motions were applied between angular steps to reduce camera pixel errors. The X-ray source was set to 100 kV and  $100 \mu\text{A}$ . 3-D reconstruction was performed using Skyscan's NRecon software with a beam hardening correction. The two scans of an individual section were combined into a single reconstruction by deleting overlapping volumes and concatenating the resul-

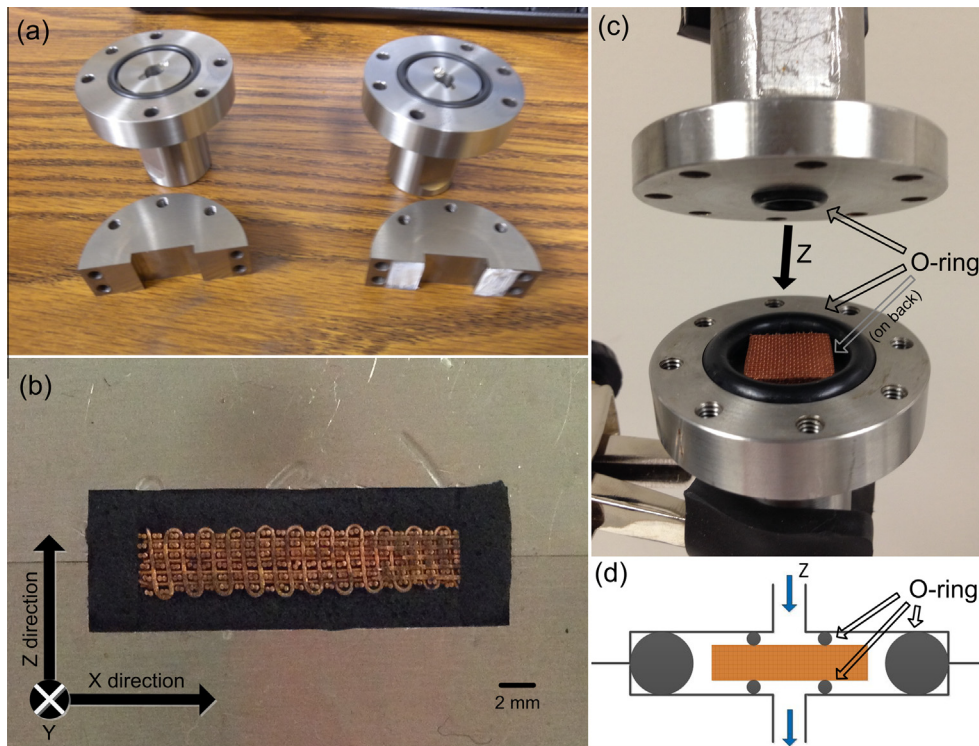


**Fig. 3.** Stainless steel fixtures for measuring permeability in the X or Y directions with closed cell foams (a, b) and in the Z direction with double O-ring system (c, d).

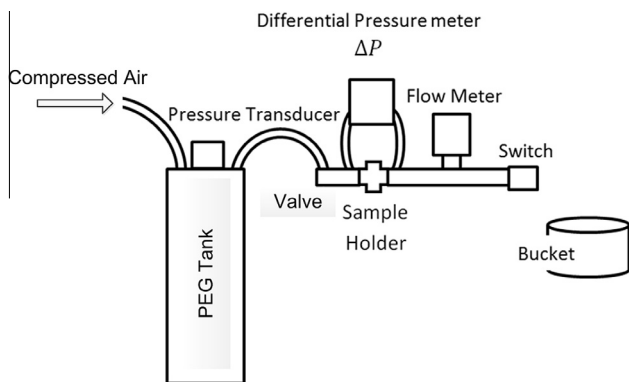


**Fig. 4.** Schematic of experimental setup for measuring permeability with PEG as the working fluid. We measure the pressure drop across the sample and flow rates through the sample.

tant files. The reconstructed volumes were binarized into two states (wire and void) using a simple threshold technique. Finally, a FE mesh was generated from the binarized data by direct voxel-to-element methodology. The mesh resolution was reduced to  $23.7 \mu\text{m}$  per element by selection of every other voxel in order to reduce the size of the model. A pressure drop, along with no-slip conditions due to the surrounding foam, were then applied to the model as boundary conditions and the resulting fluid velocity was computed to determine permeability.

### 3. Results and discussions

Prior to making extensive permeability measurements, we first examined the repeatability of these tests by

performing multiple measurements on an unbonded, optimized Cu weave sample. Pressure gradients were measured across this sample in the X, Y and Z directions while increasing and decreasing the rate of fluid flow. In addition, the sample was removed and then reinserted into the X, Y and Z holders prior to varying the rate of fluid flow. Fig. 5 illustrates that the data is very reproducible with virtually no hysteresis between increasing and decreasing the flow rates (Fig. 5a) and virtually no variation from test to test (Fig. 5b). The linear trends in Fig. 5 imply that laminar flow exists and the slopes of these lines give the ratio of viscosity over permeability ( $\mu \text{K}^{-1}$ ) from which permeability K can be calculated. The resulting permeability measurements vary by  $<1.4\%$  for Fig. 5a and  $<3.5\%$  for Fig. 5b. Even smaller variations were found for other samples. The full data set demonstrates that the measurements of permeability are very reproducible for a given sample.

In addition to characterizing the repeatability of the measurements, we also examined the impact of the silicone closed-cell foams on the permeability measurements. As shown in Fig. 3c, closed cell foams were placed around the samples when measuring permeability in the X or Y directions to ensure that fluid did not flow around the samples. These foam inserts were compressed against the samples by the stainless steel holders, thereby exerting a stress on the samples that could cause wires to shift position and alter measured permeability. To assess this potential impact, we used closed-cell foams with similar thicknesses but different buckling stresses. Thus, for the same compressive strain applied by the holders, a different compressive stress resulted on the weaves. Three different foams (PORON 4790-92 Extra Soft, PORON 4701-30 Very Soft and PORON 4701-50 Firm) were used with different stress-strain curves [54] and the applied stresses are

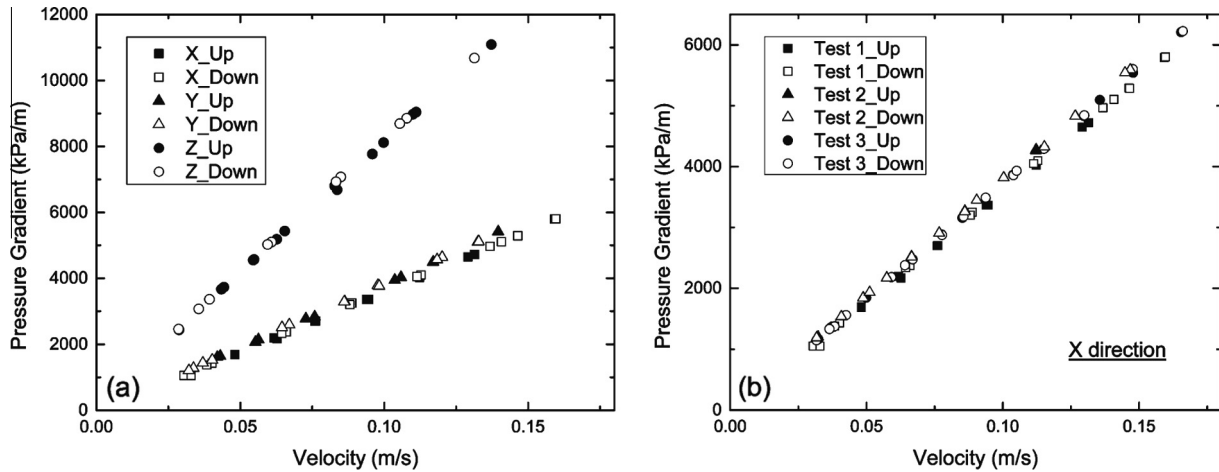


Fig. 5. Pressure gradients are measured as a function of fluid velocity through a single, unbonded, Cu optimized weave. (a) Measurements are made in all three directions on the rectangular sample, and pressure drops are measured while increasing (up) and decreasing (down) the fluid velocity. (b) Three measurements are also made on the same sample in one direction (X) after removing and reinserting the sample from/into the holder between measurements.

estimated to range from 21 kPa for the extra soft foam to 115 kPa for the firm foam. Results shown in Fig. 6 and Table 1 demonstrate that measured permeabilities do not show a difference within experimental error when varying

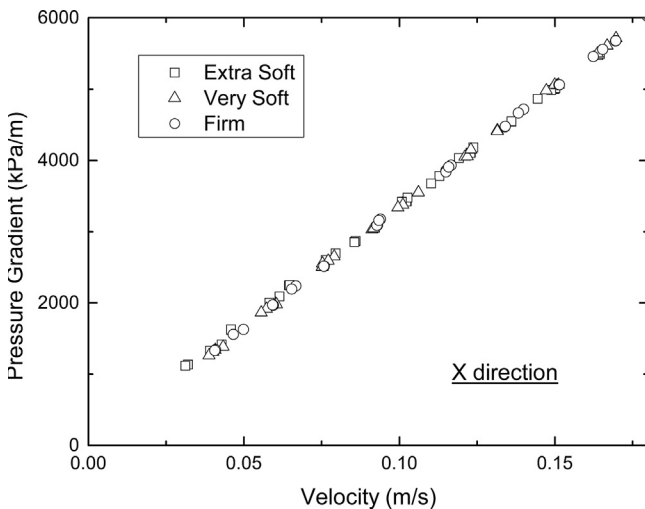


Fig. 6. Three silicone closed-cell foams were used to encapsulate optimized, unbonded Cu weaves during X direction permeability measurements to examine the influence of the pressure applied by the sealing foams. The extra soft, very soft and firm foams all had the same thickness and hence applied different normal stresses when compressed against the weaves by the stainless steel holders. The stress is estimated to have ranged from 21 to 115 kPa. All measurements were performed on the same unbonded optimized sample, with increasing and decreasing flow rates.

Table 1. Permeability as a function of foam stiffness for optimized, unbonded samples.

Foam type	Extra soft	Very soft	Firm
Strain of foam (%)	22 ± 3	20 ± 3	21 ± 3
Stress of foam (kPa) [54]	20.9 ± 1.2	33.0 ± 2.2	115.1 ± 6.7
Permeability ( $\times 10^{-10} \text{ m}^2$ )	29.8 ± 0.8	29.8 ± 0.5	29.0 ± 0.6

foam stiffness and hence applied stress. Given that the unbonded samples are the most compliant weaves, the bonded and stiffer weaves are also unlikely to show a dependence on the foam type or applied stress. In all subsequent measurements, the middle foam (PORON 4701-30 Very Soft) was used.

Fig. 7a displays plots of pressure gradients vs. fluid velocity for the unbonded standard and optimized weaves, for all three directions. Linear trends are clearly visible, as expected given the low Reynolds numbers. The slopes yield the ratio of viscosity to permeability ( $\mu \text{ K}^{-1}$ ), from which permeabilities were calculated using Darcy’s law (Eq. (1)). The resulting values are plotted in Fig. 8 for all three directions. Note that in the standard unbonded structure, permeability is relatively isotropic as it varies little with direction. This is attributed to the fact that the respective channel sizes in all three directions are relatively similar. However, for the optimized unbonded structure in which specific wires were removed, permeability increases over 600% in the X and Y directions and 200% in the Z direction. Thus, the permeability of the optimized weaves is anisotropic as designed. However, the similarity of the X and Y permeabilities was unexpected as wires were removed in a pattern to increase permeability in the X direction specifically. We attribute the unexpected change in Y to the fact that the unintended spacing in the wires due to manufacturing was larger for the Y wires than the X wires, as will be shown in the optical imaging results.

Fig. 7b displays pressure gradients measured for fluid flow in the X direction for standard and optimized samples, whose wires were bonded using different methods. All data sets show linear behavior, as in Fig. 7a, and the slopes and Eq. (1) were used to calculate permeabilities that are plotted in Fig. 8. Data for Y and Z directions are included in Fig. 8 as well; several trends appear. First, adding solder, braze or aluminum to the weaves to enable bonding between the wires reduces permeability and the largest drop is seen for soldering. The general reduction is attributed to the material volume increase due to the addition of solder, braze or aluminum, thus reducing the size of the channels. The bigger drop for soldered samples is due to the fact that a larger volume of solder was used compared to braze or

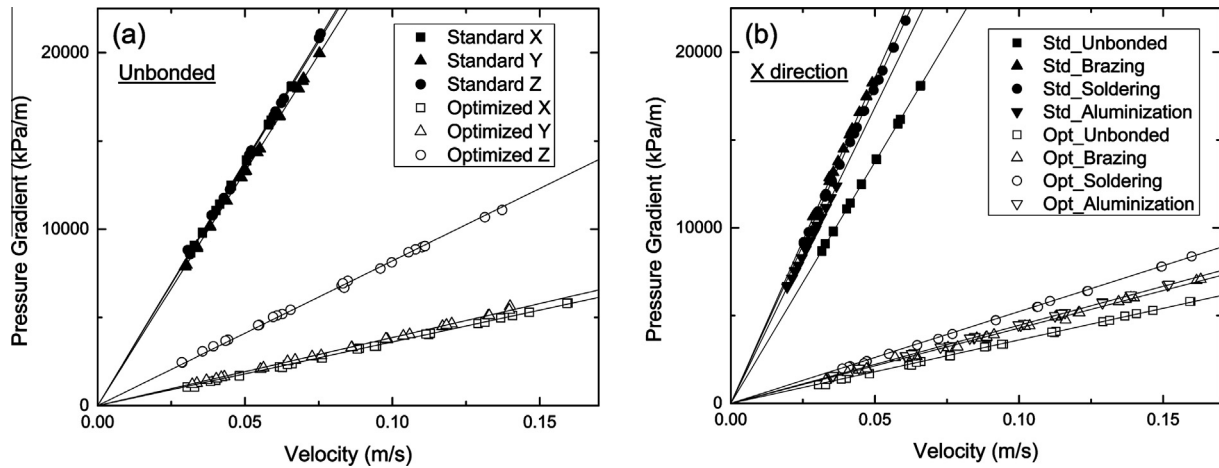


Fig. 7. (a) Permeability testing of unbonded standard and optimized Cu samples in all three directions. (b) Permeability testing of unbonded Cu, bonded Cu and Ni-20Cr, and standard (*std*) and optimized (*opt*) samples in the X direction.

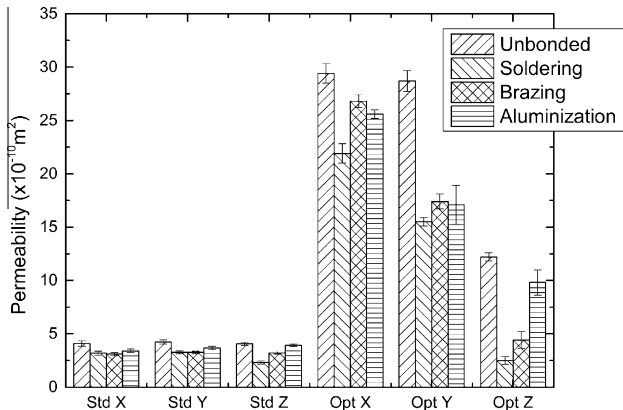


Fig. 8. Permeabilities for standard and optimized structures calculated from experimental data. Both unbonded and bonded samples are included, as well as measurements in all three directions.

aluminum. As a percentage of the weave's total volume, we estimate that the solder, braze and aluminum volumes constitute 21%, 15% and 12%, respectively, for the standard structure and 19%, 17% and 14%, respectively, for the optimized structure. In a second trend, permeability drops more in the optimized weaves than in the standard weaves following bonding. This difference may be attributed to the fact that although the relative volumes of the bonding materials are similar between the two structures, the distribution of bonding material is less uniform in the optimized structure than the standard structure given the larger distribution of pore sizes in the optimized weave. The third and final trend concerns the decrease in permeability for the X and Y directions following bonding, which is different for the standard and optimized weaves. Note that in Fig. 8, permeability drops a similar amount in the X and Y directions for the standard weaves, but decreases a much larger percentage in the Y direction than the X direction for the optimized weaves, after bonding. This can be understood by considering the pore sizes and wire patterns in the two directions. In standard samples the pattern of wires is identical in the X and Y directions, while in the optimized samples the X direction is designed to have large, winding flow

channels, resulting in the Y direction having several smaller flow channels. This leads to solder, braze or aluminum reducing channel sizes more evenly throughout X and Y directions in the standard weaves but more dramatically in the smaller Y channels in the optimized weaves.

Having tested permeabilities in all three directions for multiple samples, we now compare the measured values with FE simulations of permeability using the unit cell-based homogenization approach and the X-ray tomography-informed approach. All FE simulations use eight-node, trilinear brick elements with stabilization as described in Ref. [55], implemented in our in-house Johns Hopkins University FEM and Topology Optimization package. Details of numerical homogenization approach can be found in Ref. [40], while the tomography-informed approach is a standard single-scale FE analysis.

To perform the optimization and initial simulations, we assumed the woven structures were ideal, without flaws, as shown in Table 2. The resulting computed permeabilities in all three directions for both standard and optimized unbonded weaves are listed in Table 2. Note that with ideal, tight packing of the wires, the simulated permeabilities are much lower than the values measured for the unbonded Cu weaves. To explain this difference we first visually examined the weaves for gross flaws such as missing, extra or twisted wires, but found these were uncommon with only a few discrete defects. We then assessed the excess spacings, which are inherently introduced in the weaving process, by measuring the average spacing between X, Y and Z wires using optical microscopy (Table 3). The average excess spacing varied from 10.0 to 60.6  $\mu\text{m}$  for the standard weaves and from 9.8 to 67.7  $\mu\text{m}$  for the optimized weaves. Note also that the average spacing of the Y wires (Y–Y and Y–Z) is larger than of the X wires (X–X and X–Z), explaining the aforementioned larger than expected increase in the Y direction permeability.

As the mesh size in the 3-D FE models is 16.8  $\mu\text{m}$ , selected to balance computational expense and accurate meshing of wire cross-sections, spaces were introduced into the model in increments of the mesh size. Table 3 displays the assumed wire spacing, along with the average measured values. Numerical homogenization was then repeated using these larger, more realistic wire spacings, and the computed

**Table 2.** Finite-element simulations of permeability based on measured average excess wire spacings. All samples are unbonded Cu weaves.

Coordinates	Standard weave			Optimized weave		
	Assuming ideal wire spacings	Assuming increments in wire spacings	Measured values	Assuming ideal wire spacings	Assuming increments in wire spacings	Measured values
Increments input ( $\mu\text{m}$ )	Zero	Refer to Table 3	Refer to Table 3	Zero	Refer to Table 3	Refer to Table 3
Material fraction (%)	54.37	40.50	$42.99 \pm 7.37$	40.28	30.07	$31.52 \pm 5.23$
Permeability X ( $\times 10^{-10} \text{ m}^2$ )	0.77	3.68	$4.08 \pm 0.25$	13.55	28.66	$29.4 \pm 0.9$
Permeability Y ( $\times 10^{-10} \text{ m}^2$ )	0.79	3.88	$4.23 \pm 0.20$	9.54	20.40	$28.7 \pm 1.0$
Permeability Z ( $\times 10^{-10} \text{ m}^2$ )	0.66	3.32	$4.05 \pm 0.14$	2.03	8.74	$12.2 \pm 0.4$

**Table 3.** Measured average excess wire spacings and discretized increment for both standard and optimized structures in all three directions. The ideal weave has zero excess wire spacing. All samples are unbonded Cu weaves [41].

	Standard weave			Optimized weave		
	Wires	Average measured excess wire spacing ( $\mu\text{m}$ )	Spacing increment input for model ( $\mu\text{m}$ )	Wires	Average measured excess wire spacing ( $\mu\text{m}$ )	Spacing increment input for model ( $\mu\text{m}$ )
Spacing in X direction	Y–Y	$21.0 \pm 33.7$	16.8	Y–Y	$16.4 \pm 26.4$	16.8
	Y–Z	$60.6 \pm 41.2$	67.2	Y–Z	$67.7 \pm 14.1$	67.2
Spacing in Y direction	X–X	$10.0 \pm 9.1$	16.8	X–X	$20.7 \pm 20.0$	16.8
	X–Z	$15.9 \pm 16.6$	16.8	X–Z	$9.8 \pm 8.9$	16.8
Spacing in Z direction	Y–Z loop	$39.6 \pm 52.7$	33.6	Y–Z loop	$35.0 \pm 46.0$	33.6
	X–Y	$39.7 \pm 40.0$	33.6	X–Y	$41.9 \pm 36.2$	33.6

permeabilities fall within 29% of the measured values in all cases, as shown in Table 2. Further still, simulation results estimate that the permeability in the X direction is three times greater than the Z direction for the optimized weave, the same ratio measured in the experiments. Refinement of the mesh could lead to an even closer match of simulated and measured values. However, the use of average wire spacings will not capture local variations in wire spacing that could impact flow and hence permeability. Thus, we turned to X-ray tomography for a more accurate assessment of wire positions.

X-ray tomography was performed on an optimized Ni–20Cr specimen after aluminization. The specimen was cut from a larger sample ( $16 \times 16 \times 3.3 \text{ mm}$ ) on which permeability had been characterized and it measures only  $16 \times 5.4 \times 3.3 \text{ mm}$  as shown in Fig. 9a. This 3-D image contains 21 million finite elements (voxels) and was used to predict fluid flow in the actual structure. However, to avoid any edge effects due to cutting, we ignore the outermost unit cells along the X and Y edges. The reduced data set was then used in the FE model to simulate fluid flow and thereby predict permeability in all three directions as

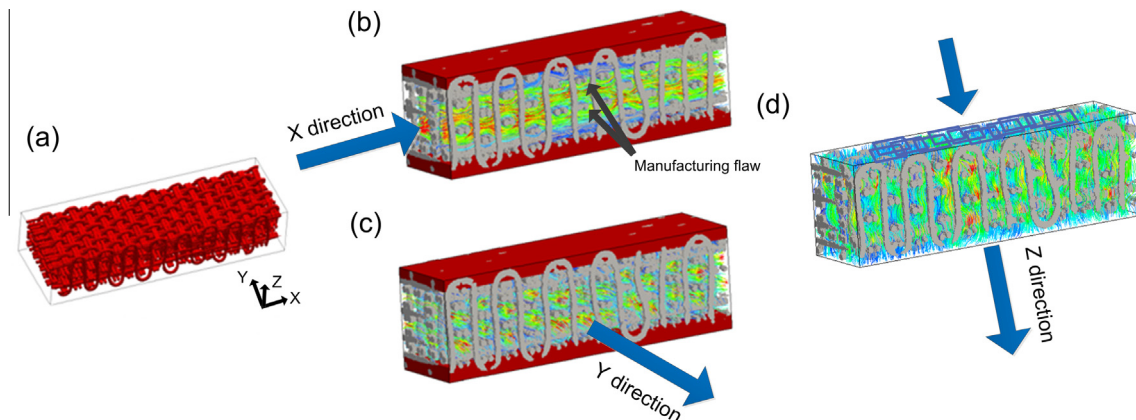


**Fig. 9.** (a) X-ray tomographic images of one-third of a Ni–20Cr sample after vapor-phase processing. (b–d) The image data is used in the FE model to simulate permeability in all three directions. Simulations in Z used the full specimen as well as smaller sections identified by the rectangles on top of the specimen in (d). A manufacturing flaw of two pairs of fill wires being placed one layer too high is identified with two arrows in (b).

shown in Fig. 9b–d. The simulated fluid velocity differs throughout the specimen, suggesting local variations in wire spacings. One particular variation in wire spacing is noted in Fig. 9b. Two arrows point to a manufacturing flaw in which the periodic variation of Ni–20Cr wires is interrupted. Throughout most of the specimen, the pairs of Y wires alternate their Z positions, creating a staggered pattern. However, in the middle of the specimen two pairs of Y wires break this pattern and are coplanar with their neighbors. Although only one such defect was observed in the NiCr sample, this manufacturing flaw reduces the local fluid flow as seen most distinctly in Fig. 9b. Such local predictions speak to the strength of X-ray tomographic data when predicting permeability.

The permeabilities predicted using the FEM and the X-ray tomography data, and those measured experimentally, are summarized in Table 4. The predictions in the X and Y directions match the experimental values well, with only a 9% difference in X and a 17% difference in Y. However, the predictions and measurements differ by 69% in the Z direction. The larger difference in the Z direction could be due to the fact that while the X-ray instrument scanned the full specimen in Fig. 9a, Z permeability was measured only in the middle section of the test sample as shown schematically in Fig. 3c and d. Thus, unlike the permeability measurements in X and Y directions, the Z measurement was not performed across the full volume of the scanned specimen, which spans the length of the test sample. To assess this possible cause of discrepancy, we estimated permeability in the Z direction using small volumes ( $3.5 \times 2.6 \times 3.3$  mm) within the scanned data that are spread across the length of the specimen and are shown schematically in Fig. 9d using blue rectangles. Using these small volumes we found that estimated permeability varied from  $11.9 \times 10^{-10}$  to  $17.8 \times 10^{-10}$  m<sup>2</sup>, a range that includes the average prediction based on the full scanned volume and almost includes the lower measured value of  $9.8 \times 10^{-10}$  m<sup>2</sup>. This suggests that differences between predicted and measured values can arise when the scanned volume differs from the tested volume and more work is needed to identify a representative volume element using the scanned data.

We end the discussion by comparing the permeability of our weaves to those of other porous structures. Pore size can vary from 75 μm for metal foams [1] to 326 μm for truss structures [56] to 1213 μm for wire screens [57]. In addition, pore fraction or material density can vary significantly [12]. Thus, when extracting measured permeabilities from the literature for comparison, we normalized measured permeabilities by the square of the characteristic pore size to achieve a dimensionless term for all structures, as was done in Ref. [1]. For our 3-D woven structures, the characteristic pore size is assumed to be the hydraulic diameter,  $D_h$ . Using unbonded Cu samples and assuming the wire spacings referred to in Table 3, the hydraulic diameters for standard

**Table 4.** Summary of experimental and simulated permeabilities for an optimized and aluminized Ni–20Cr sample.

	Experiment	X-ray tomography informed simulation
Permeability X ( $\times 10^{-10}$ m <sup>2</sup> )	$25.6 \pm 0.2$	27.9
Permeability Y ( $\times 10^{-10}$ m <sup>2</sup> )	$17.1 \pm 1.8$	14.2
Permeability Z ( $\times 10^{-10}$ m <sup>2</sup> )	$9.8 \pm 1.2$	16.6

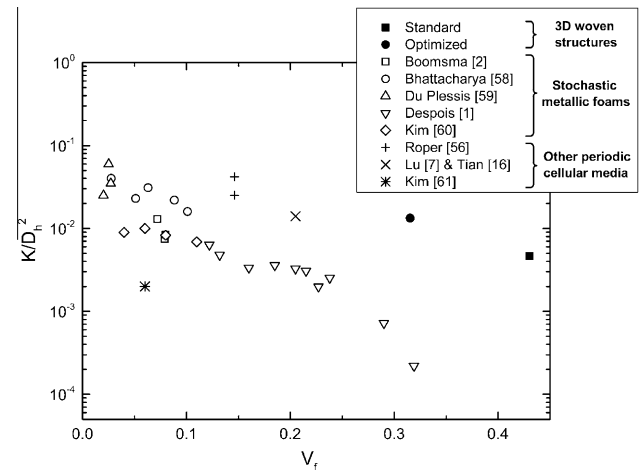


**Fig. 10.** Normalized permeability ( $K/D_h^2$ ) plotted vs. material volume fraction ( $V_f$ ) for 3-D woven structures, stochastic metallic foams and other periodic cellular media.

and optimized structures were 297 and 470 μm, respectively, as mentioned earlier in calculating the Reynolds numbers. The resulting relationships between normalized permeabilities ( $K/D_h^2$ ) and material volume fraction ( $V_f$ ) are plotted in Fig. 10 for the standard and optimized 3-D woven structures (X-direction permeability shown), stochastic metallic foams [1,2,58–60] and other periodic cellular media [7,16,56,61] including square, diamond and truss structures.

For metallic foams with stochastic structures material density is normally kept low to maintain an open pore structure. In contrast, 3-D woven structures that are more than 40% dense still maintain an interconnected pore network due to their periodic structure. As shown in Fig. 10 they offer more than a 10-fold increase in normalized permeability compared to foams with a similar volume fraction. Other periodic cellular materials, such as square, diamond and truss structures, [7,16,56,61], have similar normalized permeabilities, but their material densities tend to be much lower. The comparisons in Fig. 10 support the concept that periodic cellular materials such as 3-D weaves offer an advantage over stochastic cellular materials such as foams [1–5] in that their structures can be optimized to yield superior permeability in prescribed directions and at a given density. Further still, a combination of properties such as permeability and stiffness can be optimized [31,32]. The opportunity for such optimization will prove useful as cellular materials gain more attention in applications such as poroelastic actuators [26] or implant scaffolds [27–29].

#### 4. Conclusions

Permeability was measured for 3-D orthogonal topology-optimized Cu and Ni–20Cr woven parts under laminar flow using PEG. The permeability of standard weaves was found to be relatively isotropic with similar values measured in the X, Y and Z directions. However, when selected wires were strategically removed from the standard weave to optimize permeability in the X direction, substantial increases in permeability were obtained and the permeability became near orthotropic. Permeability increased by

600% in the X and Y directions and 200% in the Z direction. As expected, bonding the loose Cu wires using solder or braze, and loose Ni–20Cr wires using aluminum vapor, led to a decrease in permeability due to the addition of bonding material. However, permeabilities, particularly in the optimized X-direction, were still substantially larger than the standard weave architecture.

Permeability of the 3-D weaves was then predicted using FE models that included as-fabricated wire spacings. Average wire spacings were obtained from optical images, and exact wire locations were extracted from X-ray tomography. Regardless of the methods used to characterize wire spacings or locations, the resulting FEM predictions match the observed trends in permeability with direction (X, Y or Z) and design (standard vs. optimized). In addition, the absolute values of the predictions match the measured permeabilities quite well, particularly in the X and Y directions. The optical analysis provides a rapid method for assessing wire positions for predicting permeability, while the X-ray tomography data provides the additional benefit of identifying restrictions in flow that are created by local variations in wire spacing or location.

The orthogonal 3-D woven structures studied here exhibit an order of magnitude higher normalized permeability compared to stochastic porous structures with a similar material density. Compared to other periodic porous structures, the weaves showed similar normalized permeability but at substantially higher densities. In addition, the metallic weaves demonstrate a new means for fabricating structural and functional materials while leveraging topology optimization to guide the design of those materials to achieve improved sets of properties.

## Acknowledgments

This work was funded by the Defense Advanced Research Projects Agency (DARPA)—Materials with Controlled Microstructural Architecture (MCMA), under award no. W91CRB1010004 (Dr. Judah Goldwasser, program manager). The authors would like to thank Mr. Wesley Cohen for assistance during permeability testing, and Mike Franckowiak and Frank Cook for machining test fixtures.

## References

- [1] J.-F. Despois, A. Mortensen, Permeability of open-pore microcellular materials, *Acta Mater.* 53 (5) (2005) 1381–1388.
- [2] K. Boomsma, D. Poulikakos, The effects of compression and pore size variations on the liquid flow characteristics in metal foams, *J. Fluids Eng.-Trans. ASME* 124 (1) (2002) 263–272.
- [3] T. Lu, H. Stone, M. Ashby, Heat transfer in open-cell metal foams, *Acta Mater.* 46 (10) (1998) 3619–3635.
- [4] K. Boomsma, D. Poulikakos, F. Zwick, Metal foams as compact high performance heat exchangers, *Mech. Mater.* 35 (12) (2003) 1161–1176.
- [5] V.V. Calmide, R.L. Mahajan, Forced convection in high porosity metal foams, *J. Heat Transfer* 122 (3) (2000) 557–565.
- [6] L. Valdevit et al., Optimal active cooling performance of metallic sandwich panels with prismatic cores, *Int. J. Heat Mass Transf.* 49 (21–22) (2006) 3819–3830.
- [7] T.J. Lu, L. Valdevit, A.G. Evans, Active cooling by metallic sandwich structures with periodic cores, *Prog. Mater. Sci.* 50 (7) (2005) 789–815.
- [8] J. Tian et al., Cross flow heat exchange of textile cellular metal core sandwich panels, *Int. J. Heat Mass Transf.* 50 (13–14) (2007) 2521–2536.
- [9] D.T. Queheillalt, H.N.G. Wadley, Cellular metal lattices with hollow trusses, *Acta Mater.* 53 (2) (2005) 303–313.
- [10] Y.-H. Lee et al., Wire-woven bulk Kagome truss cores, *Acta Mater.* 55 (18) (2007) 6084–6094.
- [11] K.-J. Kang, A wire-woven cellular metal of ultrahigh strength, *Acta Mater.* 57 (6) (2009) 1865–1874.
- [12] C.S. Roper, Multiobjective optimization for design of multifunctional sandwich panel heat pipes with micro-architected truss cores, *Int. J. Heat Fluid Flow* 32 (1) (2011) 239–248.
- [13] R.A. Wirtz et al., Thermal/fluid characteristics of 3-D woven mesh structures as heat exchanger surfaces, *IEEE Trans. Compon. Packag. Technol.* 26 (1) (2003) 40–47.
- [14] J.-W. Park, D. Ruch, R. Wirtz, Thermal/fluid characteristics of isotropic plainweave screen laminates as heat exchange surfaces, *AIAA Paper* 208 (2002) 2002.
- [15] M. Zupan, V.S. Deshpande, N.A. Fleck, The out-of-plane compressive behaviour of woven-core sandwich plates, *Eur. J. Mech. – A/Solids* 23 (3) (2004) 411–421.
- [16] J. Tian et al., The effects of topology upon fluid-flow and heat-transfer within cellular copper structures, *Int. J. Heat Mass Transf.* 47 (14–16) (2004) 3171–3186.
- [17] V.S. Deshpande, N.A. Fleck, High strain rate compressive behaviour of aluminium alloy foams, *Int. J. Impact Eng.* 24 (3) (2000) 277–298.
- [18] I.W. Hall, M. Guden, C.J. Yu, Crushing of aluminum closed cell foams: density and strain rate effects, *Scr. Mater.* 43 (6) (2000) 515–521.
- [19] M.F. Ashby, R.F.M. Medalist, The mechanical properties of cellular solids, *Metall. Trans. A* 14 (9) (1983) 1755–1769.
- [20] L.J. Gibson, Mechanical behavior of metallic foams, *Annu. Rev. Mater. Sci.* 30 (1) (2000) 191–227.
- [21] A.G. Evans, J.W. Hutchinson, M.F. Ashby, Multifunctionality of cellular metal systems, *Prog. Mater. Sci.* 43 (3) (1998) 171–221.
- [22] A.G. Evans et al., The topological design of multifunctional cellular metals, *Prog. Mater. Sci.* 46 (3–4) (2001) 309–327.
- [23] A.G. Evans, J.W. Hutchinson, M.F. Ashby, Cellular metals, *Curr. Opin. Solid State Mater. Sci.* 3 (3) (1998) 288–303.
- [24] K.J. Maloney et al., Multifunctional heat exchangers derived from three-dimensional micro-lattice structures, *Int. J. Heat Mass Transf.* 55 (9–10) (2012) 2486–2493.
- [25] H.N.G. Wadley, Multifunctional periodic cellular metals, *Philos. Trans. R. Soc. A: Math. Phys. Eng. Sci.* 2006 (364) (1838) 31–68.
- [26] C.S. Andreasen, O. Sigmund, Saturated poroelastic actuators generated by topology optimization, *Struct. Multidiscip. Optim.* 43 (5) (2011) 693–706.
- [27] S.J. Hollister, Porous scaffold design for tissue engineering, *Nat. Mater.* 4 (7) (2005) 518–524.
- [28] S.J. Hollister, Scaffold design and manufacturing: From concept to clinic, *Adv. Mater.* 21 (32–33) (2009) 3330–3342.
- [29] V.J. Challis et al., Prototypes for bone implant scaffolds designed via topology optimization and manufactured by solid freeform fabrication, *Adv. Eng. Mater.* 12 (11) (2010) 1106–1110.
- [30] A.P. Fraas, *Heat Exchanger Design*, John Wiley, New York, 1989.
- [31] V.J. Challis et al., Computationally generated cross-property bounds for stiffness and fluid permeability using topology optimization, *Int. J. Solids Struct.* 49 (23–24) (2012) 3397–3408.
- [32] J.K. Guest, J.H. Prevost, Optimizing multifunctional materials: Design of microstructures for maximized stiffness and fluid permeability, *Int. J. Solids Struct.* 43 (22–23) (2006) 7028–7047.
- [33] R. Lotfi et al., Topology optimization for cellular material design, in: *MRS Proceedings*, Cambridge University Press, Cambridge, 2014.
- [34] M.H. Mohamed, M.M. Salama, High speed three-dimensional weaving method and machine. US Patent 6,315,007, 2001.

- [35] M. Mohamed, A. Bogdanovich, Comparative analysis of different 3D weaving processes, machines and products, in: Proceedings of the 17th International Conference on Composite Materials (ICCM-17), 2009.
- [36] O. Sigmund, Materials with prescribed constitutive parameters: An inverse homogenization problem, *Int. J. Solids Struct.* 31 (17) (1994) 2313–2329.
- [37] J.K. Guest, J.H. Prévost, T. Belytschko, Achieving minimum length scale in topology optimization using nodal design variables and projection functions, *Int. J. Numer. Meth. Eng.* 61 (2) (2004) 238–254.
- [38] J.K. Guest, Topology optimization with multiple phase projection, *Comput. Meth. Appl. Mech. Eng.* 199 (1–4) (2009) 123–135.
- [39] S.-H. Ha, J. Guest, Optimizing inclusion shapes and patterns in periodic materials using Discrete Object Projection, *Struct. Multidiscip. Optim.* 50 (1) (2014) 65–80.
- [40] J.K. Guest, J.H. Prevost, Design of maximum permeability material structures, *Comput. Meth. Appl. Mech. Eng.* 196 (4–6) (2007) 1006–1017.
- [41] Y. Zhang et al., Fabrication and mechanical characterization of 3D woven Cu lattice materials, to be submitted, 2014.
- [42] Arcor Electronics Uninsulated Wire: <<http://www.arcorelectronics.com/uninsulated-wire/>>.
- [43] Indium Corporation Pb-Free Alloys for Solder Paste: <<http://www.indium.com/solder-paste-and-powders/leading-pb-free-solder-pastes/#products>>.
- [44] Lucas-Milhaupt Alloy for Brazing: <<http://www.lucasmilhaupt.com/en-US/knowledgebase/technicalmsdsdocuments/>>.
- [45] D. Erdeniz, D.C. Dunand, Microstructure development during pack aluminization of nickel and nickel–chromium wires, *Intermetallics* 50 (2014) 43–53.
- [46] H. Choe, D.C. Dunand, Synthesis, structure, and mechanical properties of Ni–Al and Ni–Cr–Al superalloy foams, *Acta Mater.* 52 (5) (2004) 1283–1295.
- [47] G.W. Goward, D.H. Boone, Mechanisms of formation of diffusion aluminide coatings on nickel-base superalloys, *Oxid. Met.* 3 (5) (1971) 475.
- [48] G.W. Goward, L.W. Cannon, Pack cementation coatings for superalloys - a review of history, theory, and practice, *J. Eng. Gas Turbines Power-Trans. ASME* 110 (1) (1988) 150–154.
- [49] D.E. Burns et al., Development of Ni-based superalloys for microelectromechanical systems, *Scr. Mater.* 67 (5) (2012) 459–462.
- [50] A.M. Hodge, D.C. Dunand, Synthesis of nickel–aluminide foams by packaluminization of nickel foams, *Intermetallics* 9 (7) (2001) 581–589.
- [51] D.C. Dunand, A.M. Hodge, C. Schuh, Pack aluminisation kinetics of nickel rods and foams, *Mater. Sci. Technol.* 18 (3) (2002) 326–332.
- [52] D. Erdeniz et al., Pack aluminization synthesis of superalloy 3D woven and 3D braided structures, *Metall. Mater. Trans. A* (2014), submitted for publication.
- [53] E. Sanchez-Palencia, Non-homogeneous media and vibration theory, *Non-homogeneous Media and Vibration Theory. Lecture Notes in Physics*, vol. 127, Springer Verlag, Berlin, 1980.
- [54] PORON Urethane Compression Force Deflection Curves: <<http://www.rogerscorp.com/documents/927/hpf/poron/industrial/PORON-Urethane-Compression-Force-Deflection-CFD-Curves.pdf>>.
- [55] T.J.R. Hughes, L.P. Franca, M. Balestra, A new finite-element formulation for computational fluid-dynamics .5. Circumventing the Babuska-Brezzi condition - a Stable Petrov-Galerkin formulation of the Stokes Problem accommodating equal-order interpolations, *Comput. Meth. Appl. Mech. Eng.* 59 (1) (1986) 85–99.
- [56] C.S. Roper et al., Anisotropic convective heat transfer in microlattice materials, *AIChE J.* 59 (2) (2013) 622–629.
- [57] C.-T. Hsu, H. Fu, P. Cheng, On pressure-velocity correlation of steady and oscillating flows in regenerators made of wire screens, *J. Fluids Eng.* 121 (1) (1999) 52–56.
- [58] A. Bhattacharya, V.V. Calmidi, R.L. Mahajan, Thermophysical properties of high porosity metal foams, *Int. J. Heat Mass Transf.* 45 (5) (2002) 1017–1031.
- [59] P. Du Plessis et al., Pressure drop prediction for flow through high porosity metallic foams, *Chem. Eng. Sci.* 49 (21) (1994) 3545–3553.
- [60] S.Y. Kim, J.W. Paek, B.H. Kang, Flow and heat transfer correlations for porous fin in a plate-fin heat exchanger, *J. Heat Transfer* 122 (3) (2000) 572–578.
- [61] T. Kim, H.P. Hodson, T.J. Lu, Fluid-flow and endwall heat-transfer characteristics of an ultralight lattice-frame material, *Int. J. Heat Mass Transf.* 47 (6–7) (2004) 1129–1140.